

Microphysical Characterization of Microwave Radar Reflectivity Due to Volcanic Ash Clouds

Frank Silvio Marzano, *Senior Member, IEEE*, Gianfranco Vulpiani, and William I. Rose

Abstract—Ground-based microwave radar systems can have a valuable role in volcanic ash cloud monitoring as evidenced by available radar imagery. Their use for ash cloud detection and quantitative retrieval has been so far not fully investigated. In order to do this, a forward electromagnetic model is set up and examined taking into account various operating frequencies such as S-, C-, X-, and Ka-bands. A dielectric and microphysical characterization of volcanic vesicular ash is carried out. Particle size-distribution (PSD) functions are derived both from the sequential fragmentation-transport (SFT) theory of pyroclastic deposits, leading to a scaled-Weibull PSD, and from more conventional scaled-Gamma PSD functions. Best fitting of these theoretical PSDs to available measured ash data at ground is performed in order to determine the value of the free PSD parameters. The radar backscattering from spherical-equivalent ash particles is simulated up to Ka-band and the accuracy of the Rayleigh scattering approximation is assessed by using an accurate ensemble particle scattering model. A classification scheme of ash average concentration and particle size is proposed and a sensitivity study of ash radar backscattering to model parameters is accomplished. A comparison with C-band radar signatures is finally illustrated and discussed.

Index Terms—Ash clouds, microwave radars, radar remote sensing, volcanic eruption.

I. INTRODUCTION

THE detection and quantitative retrieval of volcanic ash clouds is of significant interest due to its environmental and socio-economic effects [1]–[3]. Ash fallout can cause substantial hardship and damages in volcano's surrounding area and represents a serious hazard to aircrafts as well [4], [5]. Real-time aerial mapping of a volcanic eruption, in terms of its intensity and dynamics, is usually not possible by conventional visual inspection, especially during poor visibility expected in those circumstances [6].

In order to monitor ash cloud patterns, aircraft observations have a limited value, due to their nonsystematic nature and inherent hazards for flights within an ash cloud [7], [8]. In this respect satellite measurements can offer the advantage of a global coverage with a known temporal repeatability [9]. Satellite visible-infrared radiometric observations from geostationary

satellites (e.g., Meteosat sensors) are usually exploited for long-range trajectory tracking and for measuring low level eruptions [10]–[12]. Their imagery is available every 15–30 min and suffers from a relatively poor spatial resolution (i.e., order of some kilometers). Moreover, the field of view of geostationary radiometric measurements may be blocked by water and ice clouds at higher levels and their overall utility is reduced at night [13]. Satellite data from radiometric sensors aboard near-polar orbiting platforms, such as the Advanced Very High Resolution Radiometer (AVHRR) aboard the National Oceanic Atmospheric Administration's Television Infrared Observation Satellite (TIROS), the Total Ozone Monitoring System (TOMS) aboard the Landsat platform, and the Moderate Resolution Imaging Spectrometer (MODIS) aboard the Terra platform, can also be employed to detect and map volcanic ash clouds over the entire globe [14]–[17]. The usefulness of these sensors is limited by their relatively poor temporal resolution guaranteeing only two overpasses per day at most using a single platform. More recently spaceborne microwave radiometric data have been also investigated for ash cloud retrieval, even though their spatial resolution is of the order of several tens of kilometers [18].

It should be noted that many volcanic cloud encounters have happened only minutes to a few hours after eruptive events so that timely information on the eruption's onset and its intensity is vital [4]–[8]. Among the remote sensors, ground-based microwave weather radars may represent an important tool to detect and, to a certain extent, mitigate the hazard from the ash clouds [19]–[23]. The possibility of monitoring 24 hours a day, in all weather conditions, at a fairly high spatial resolution (less than few hundreds of meters) and every few minutes after the eruption is the major advantages of using ground-based microwave radar systems. Ground-based weather radar systems can also provide data for determining the ash volume, total mass and height of eruption clouds. The latter information is especially valuable because a series of column height measurements allows the mass and dynamics of an eruption to be directly monitored. Moreover, the altitude of the cloud top above the vent represents an essential datum both to aviation safety and early warning and to ash cloud trajectory models able to forecast the position of volcanic clouds after an eruption based on winds aloft [24], [25]. In this respect, other ground-based microwave instrumentation, such as global positioning system (GPS) receivers and wind profiler radars, may play a complementary role for monitoring volcanic cloud evolution, even though their operational utility is limited by the relatively small spatial coverage (e.g., [26] and [27]). On the other hand, ground-based lidar optical systems may show a higher sensitivity to ash contents with respect to microwave instruments, but counterbalanced by stronger path attenuation effects (e.g., [28]).

Manuscript received July 22, 2005; revised September 20, 2005. This work was supported in part by the Italian Ministry of University and Research.

F. S. Marzano is with the Department of Electronic Engineering, University "La Sapienza" of Rome, 00184 Rome, Italy and also with CETEMPS, University of Aquila, 67040 L'Aquila, Italy (e-mail: marzano@die.uniroma1.it).

G. Vulpiani is with CETEMPS, University of L'Aquila, 67040 L'Aquila, Italy (e-mail: g.vulpiani@aquila.infn.it).

W. I. Rose is with the Department of Geological Engineering and Sciences, Michigan Technological University, Houghton, MI 49931 USA (e-mail: raman@mtu.edu).

Digital Object Identifier 10.1109/TGRS.2005.861010

In spite of this potential and the fact that weather radar use dates back to early eighties, there are still open issues about microwave weather radar capabilities to quantitatively retrieve volcanic ash cloud parameters [29]–[32]. Single-polarization Doppler radars can measure horizontally polarized power echo and Doppler frequency shift from which ash content and radial velocity can be revealed. Several unknowns condition the accuracy of radar products, most of them related to the microphysical variability of ash clouds such as their particle size distribution, shape, and dielectric composition [33]–[36]. Even though this variability cannot be fully resolved by using the available observables of Doppler microwave radars, the accuracy of radar remote sensing of volcanic eruptions can be quantitatively assessed by estimating the uncertainty of microphysical and scattering models of ash clouds.

In this work, the potential of using ground-based weather radar systems for volcanic ash cloud detection, and quantitative retrieval is evaluated from a modeling point of view. In order to do this, microwave radar sensitivity to ash clouds is examined taking into account various operating frequencies such as S-, C-, X-, and Ka-bands. Experimental evidences, concerning weather radar detectability of ash clouds during major volcano eruptions, are summarized in Section II. Afterward, the dielectric and microphysical characterization of volcanic ash is mainly carried out within Section III in terms of modeled particle size-distribution (PSD) functions. The latter are expressed by means of two different analytical models, the scaled-Gamma PSD and the scaled-Weibull PSD as in Appendix A. The radar backscattering from spherical-equivalent ash particles is simulated under Rayleigh approximation up to Ka-band, and its accuracy is assessed by using an accurate backscattering model in Section IV. A systematic sensitivity analysis is carried out by varying ash concentration, ash-fall regimes, and model parameters. Finally, a summary and recommendations for the development of volcanic ash radar retrieval algorithms are given in the conclusion.

II. VOLCANIC ASH AND RADAR REMOTE SENSING

Materials of all types and sizes that erupt from a crater or volcanic vent as a result of an intensive magma and rock fragmentation are usually referred to as tephra [1]–[3]. Among tephra, volcanic ash is made by small particles (<2 mm in average diameter) of pulverized rock blown from an explosion vent. Ash clouds are transported and their particles are sorted by prevailing winds and eventually fall through the air (ashfall) resulting in a deposit that is well sorted and layered.

Volcanic ash is formed by volcanoes through several different processes that transform large batches of magma and country rock into smaller pieces [33]. Two general mechanisms can be identified: 1) magmatic fragmentation in which the evolution and expansion of magmatic gases contribute to volcanic ash production; ash particles are usually marked by the presence of vesicles and production of pumice; 2) hydrovolcanic (also called phreato-magmatic) fragmentation in which physical contact and mixing of magma with external water result in ash particle formation; the propagation of stress waves through the magma and instabilities at the interfaces between magma and water can contribute to ash production.

Ash cloud particles consist mainly of angular shattered rock fragments and have a quite irregular and complex shape [35].

They can be categorized as vesicular, nonvesicular, and miscellaneous. The diameters of particles in fall deposits typically range from a few microns or less to several centimeters or more. Both the concentration and diameter of particles in the volcanic clouds decrease with distance from the vent because larger particles tend to fall out quickly [36]. Generally, finer particles (< 10 μm in average diameter) can stay suspended for days to months and can be transported to great distances from the volcanic source. Analogously, coarse ash (< 64 μm in average diameter) may have a relatively long atmospheric residence time (more than several hours) [3], whereas lapilli (>1 mm in average diameter) tend to fall out within an hour [34]. Bombs or blocks (>64 mm) across ejected by the explosion typically fall within a few kilometers of the eruption site very rapidly (within few minutes).

It is worth mentioning that, with respect to rainfall, ashfall has some important differences [9]: 1) ashfall amounts and size distributions are preserved for very long periods (until millions of years) after deposition, except for aggregation of fine ash; 2) the ash PSD is mainly established by explosive fragmentation rather than by reversible processes such as condensation, evaporation, coalescence, and breakup. In contrast with rain clouds, since ash clouds can be a major hazard to air flights, *in situ* sampling of ash clouds by aircraft is not possible except during very light ashfall. The use of the radar to observe ash eruptions is quite limited, indeed, and most radar observations of volcanic eruptions are occasionally carried out by meteorological radars of national weather services. In 1970, the tephra from Hekla volcano was first observed in Iceland, while in the U.S., first radar observations were performed during the eruption of Augustine volcano in Alaska in 1976. During Mount Saint Helens activity of 1980–1982 there was the unique opportunity to collect observations using the U.S. National Weather Service radar system at C-band in Portland, OR. These results were reported in detail by Harris and Rose [20] and Krohn and Lemon [21]. There are other examples of volcanic ash detected by ground-based weather radars from 1970 to nowadays [50], and the most important of them are listed in Table I.

Some recent episodes of volcanic ash radar detection are qualitatively illustrated in Figs. 1 and 2. Fig. 1 shows the eruptions of Soufriere Hills volcano, that occurred on March 20, 2000 [38] and monitored by an S-band radar located at Guadalupe Island. Note that horizontally polarized reflectivity data, as usual, are calibrated with the dielectric factor of water (i.e., equal to 0.93; see Fig. 8 and related comments for further details). Due to the distance between radar and volcano (about 100 km) it is a remarkable example of capability of S-band weather to detect ash cloud with reflectivity values up to 55 dBZ near the volcano vent mainly due to coarse ash and lapilli ejection.

Another example is the radar observation of the Mount Etna eruption that began on October 27, 2002 (e.g., [32]). This eruption resulted in the total destruction of the tourist complex and skiing area and a portion of a pine forest. Eruptive activity on the northeastern flank produced the main lava flows and ended on November 5, while less lava but a large volume of pyroclastics was produced on the southern flank with an activity that continued until November 16, 2002. Heavy ash falls mostly affect the Catania area, repeatedly forcing the closure of Catania airport. Eruptive seismicity and ground deformation caused damage on the northeastern and eastern

TABLE I
REPORTED ASH CLOUD ECHO DETECTION BY GROUND-BASED WEATHER
RADARS DURING MAJOR VOLCANIC ERUPTIONS BETWEEN 1970
AND 2004 (BASED ON THE LIST OF SAWADA, 2004 [50])

Year	Volcano	Zone, STATE
1970	Hekla	ICELAND
1973	Chaca	Kunashiri Islands, JAPAN
1976	Augustine	Alaska, USA
1977	Usu	Hokkaido, JAPAN
1980	Mount St. Helens	Washington, USA
1981	Hekla	ICELAND
1981	Pagan	Mariana Islands, MICRONESIA
1984	Sakura-jima	Kyushu, JAPAN
1986	Izu-Oshima	Izu-Islands, JAPAN
1991	Pinatubo	PHILIPPINES
1991	Hekla	ICELAND
1991	Unzen	Kyushu, JAPAN
1992	Spurr	Alaska, USA
1992	Pinatubo	PHILIPPINES
1992	Unzen	Kyushu, JAPAN
1993	Unzen	Kyushu, JAPAN
1996	Sakura-jima	Kyushu, JAPAN
1998	Popocatepetl	MEXICO
1999	Popocatepetl	MEXICO
2000	Miyake-jima	Izu-Islands, JAPAN
2000	Hekla	ICELAND
2000	Soufriere Hills	Montserrat Island CARRAIBEN
2002	Etna	Sicily, ITALY
2004	Grimsvotn	ICELAND

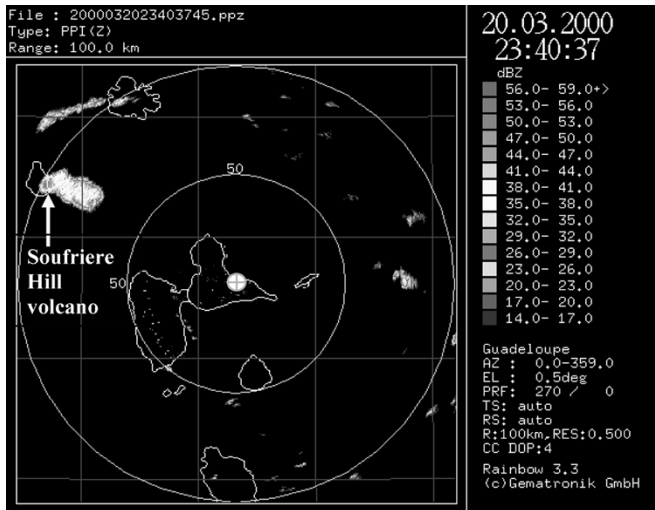


Fig. 1. Plan position indicator (PPI) of horizontally polarized radar reflectivity factor (dBZ), measured by S-band weather radar of Guadeloupe during the Soufriere Hill volcano eruption on March 20, 2000 at 23:405 UTC (courtesy of AMS-Gematronik and Météo France, Guadeloupe). Volcano vent is indicated by an arrow and radar location by a circle. Reflectivity data are calibrated with water dielectric factor (i.e., $|K|^2 = 0.93$; see text for details).

flanks. The total estimated lava volume was about 10.5 Mm^3 , while tephra volume was larger than 20 Mm^3 . As shown in Fig. 2, C-band radar images were taken from U.S. Navy station of Sigonella (Sicily, Italy), about 40 km far from the vent [39]. In this case, due to widespread meteorological clouds over Sicily, the Meteosat geostationary satellite couldn't map the ash eruption, while the C-band radar clearly detected the ash cloud dispersion. In this snapshot, observed reflectivity values were not higher than 30 dBZ due to the fact the ash cloud was

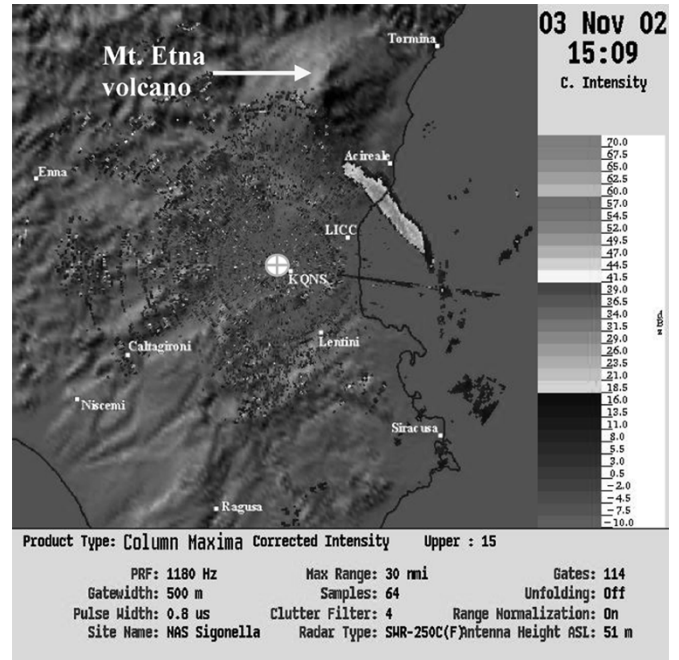


Fig. 2. PPI of horizontally polarized radar reflectivity factor (dBZ, named also corrected intensity), measured by C-band weather radar of Sigonella (Sicily, Italy) during Mount Etna volcano eruption on November 03, 2002 at 15:09 UTC (courtesy of NATO Sigonella base, Italy). Volcano vent is indicated by an arrow and radar location by a circle. Reflectivity data are calibrated with water dielectric factor (i.e., $|K|^2 = 0.93$; see text for details).

already relatively far (about 10 km) from the volcano vent and mainly constituted by fine and coarse ash.

As a further recent example, the Hekla eruption that began on February 26, 2000 was continuously and completely monitored by a C-band weather radar located about 140 km far from volcano. Ash cloud observations and volcanological interpretation are well described by Lacasse *et al.* [31]. A final remarkable example on the use of an X-band polarimetric radar is the observation of volcanic ash cloud at a distance of about 40 km from Mount Oyama volcano in Japan. More details on this case study can be found in [29].

III. MICROPHYSICAL MODEL OF VOLCANIC ASH RADAR REFLECTIVITY

In the following paragraphs, quantitative definitions and physical parameterization of volcanic ash clouds will be briefly described together with some radar reflectivity modeling issues.

A. Volcanic Ash Parameterization

The particle size distribution provides a description of the particle occurrence per unit volume and unit size (typically expressed as per centimeter to the fourth (cm^{-4}) or per cubic meter per millimeter ($\text{m}^{-3} \cdot \text{mm}^{-1}$)). As known, PSD plays a significant role in determining the backscattering and absorption properties of a particle ensemble [40], [41]. Here the ash PSD will be indicated either by $N_a(D)$ where D [mm] is the particle diameter or by $N_a(\phi)$ where ϕ is the so-called ϕ unit defined as [41]

$$\phi \equiv -\log_2 \left(\frac{D}{D_r} \right) \quad (1)$$

where conventionally $D_r = 1$ mm. The use of ϕ -unit is historically justified in volcanology by conventional plots in a base-2 logarithmic scale. A general scaled form of $N_a(D)$ [$\text{m}^{-3} \cdot \text{mm}^{-1}$] has been assumed in this work to describe ash PSD, formally expressed by

$$N_a(D) = N_n \left(\frac{D}{D_n} \right)^\mu e^{-\Lambda_n \left(\frac{D}{D_n} \right)^\nu} \quad (2)$$

where D_n [mm] is the number-weighted mean diameter and, in a logarithmic plane, N_n [$\text{m}^{-3} \cdot \text{mm}^{-1}$] is the intercept, Λ_n is the slope, μ is the shape factor and ν the slope factor. The normalization is such that N_n and Λ_n are related to the mean diameter D_n and ash concentration C_a and have physical dimensions independent on μ and ν . Bimodal PSDs have been also estimated from the analysis of ground ash samples, but here a simple unimodal form, like (2), has been adopted considering it a more consolidated assumption of average size distributions [37].

The PSD form, given in (2), is quite general, and its derivation is detailed in Appendix A. It is demonstrated that (2) may represent both the scaled-Weibull PSD (SW-PSD) and the scaled-Gamma PSD (SG-PSD). In particular, the scaled-Gamma is derived from the analogous form established for raindrops [41], while the scaled-Weibull PSD is shown to be a derivation from the sequential fragmentation-transport (SFT) theory where particle transport and growth are taken into account in a physical manner [33], [42], [43]. As outlined in Appendix A, the maximum-likelihood best fitting of (2) with respect to available PSD ash measurements has shown that the most probable value of μ is about 1 and 0.5 for a scaled-Gamma and scaled-Weibull PSD, respectively. For instance, from (A.4) the parameters of ash scaled-Gamma PSD for $\mu = 1$ take the following simple form:

$$N_{nG} = \frac{8D_n^{-5}}{\pi\rho_a} C_a \quad \Lambda_{nG} = 2. \quad (3)$$

Similar expressions can be derived for scaled-Weibull PSD. Note that, in case of SW-PSD, we will indifferently refer to either $\mu = 0.5$ or $\gamma = -0.5$ with $\nu = \mu + 1$ in (2) (see Appendix A).

In Section II the shape of ash particles has been briefly discussed. Experimental evidence shows that ash and lapilli and their aggregates can be only roughly approximated by a spherical shape [35]. However, most ash shape measurements refer to distal volcanic ash deposit at ground so that properties of suspended and falling ash can be only inferred. The spherical shape assumption is widely used in radiative modeling for remote sensing purposes (e.g., [15], [20], and [29]). These considerations have prompted us to consider, as a first approximation, ash clouds as a collection of randomly distributed spherical particles. Their composition may be assumed to be a mixture of solid ash and air in order to take into account their vesicular nature. Analysis of ash mixtures with water in vapor, ice, and liquid phase are beyond the scope of this work.

From the knowledge of the ash particle distribution, shape, and density, some meaningful physical parameters can be introduced. For a spherical particles, the ash particle mass m_a [kg] will be given by

$$m_a(D) = \frac{\pi}{6} \rho_a(D) D^3 \quad (4)$$

where ρ_a [$\text{g} \cdot \text{m}^{-3}$] is the ash density which will be assumed independent of diameter in the next formulas, if not otherwise stated. Values of ρ_a may range from 0.5 for magmatic ash to $2.5 \text{ g} \cdot \text{cm}^{-3}$ for highly vesicular pumice [1], [20]. If the (incomplete) moment m_n of order n of N_a is expressed by

$$m_n = \int_{D_1}^{D_2} D^n N_a(D) dD \quad (5)$$

where D_1 and D_2 are the minimum and maximum diameters, respectively, then the following definitions hold.

- *Total volumetric number:* N_t [m^{-3}] of ash particles, i.e., total number per unit volume, given by

$$N_t \equiv \int_{D_1}^{D_2} N_a(D) dD = m_0. \quad (6)$$

- *Mass concentration:* C_a [$\text{g} \cdot \text{m}^{-3}$] of sphere-equivalent ash particles, given by

$$C_a \equiv \int_{D_1}^{D_2} m_a(D) N_a(D) dD = \frac{\pi}{6} \rho_a m_3. \quad (7)$$

- *Number-weighted mean diameter:* D_n [mm], defined by

$$D_n = \frac{\int_{D_1}^{D_2} D N_a(D) dD}{\int_{D_1}^{D_2} N_a(D) dD} = \frac{m_1}{m_0}. \quad (8)$$

The ashfall rate R_a can be also defined in terms of m_n once known the terminal fall velocity $v_a(D)$ in still air of ash particles and w_{up} the vertical component of the air speed. The estimate of $v_a(D)$, approximated by a power law and dependent on height and particle shape, is generally done by means of empirical analyses [20], [32], [45]. Finally, it may be useful to give the explicit expression of the complete moments (i.e., when $D_1 = 0$ and $D_2 = \infty$), for instance in case of SG-PSD with $\mu = 1$

$$m_{nG} = \frac{N_{nG}}{(\Lambda_{nG})^{n+2}} D_n^{n+2-\mu} \Gamma(n+2) = \frac{\Gamma(n+2)}{2^{n-1}\pi} \frac{C_a}{\rho_a} D_n^{n-3} \quad (9)$$

where Γ is the Gamma function and N_{nG} and Λ_{nG} are derived from (3) in the last term. A similar expression can be given for SW-PSD.

B. Radar Reflectivity and Its Approximations

As discussed in Section II, volcanic ash clouds can be considered radar targets similar to rainfall due to the backscatter of the transmitted power incident on particle polydispersion within the radar resolution volume. Both rain and ash cloud fractional volumes are so low (less than few percent) to allow independent scattering hypotheses to be applied for backscattered power computation. Thus, the theory governing radar backscattering from rain targets may be applied to radar reflections from ash cloud with obvious differences.

For single-polarization Doppler radars, the horizontally polarized radar reflectivity η_H [m^{-1}] at the bin range r is given by [40], [41]

$$\eta_H = \int_{D_1}^{D_2} \sigma_{bH}(D) N_a(D) dD = \frac{\pi^5 |K_a|^2}{\lambda^4} Z_H \quad (10)$$

where σ_{bH} [m^2] is the backscattering cross section at horizontal polarization, λ is the radar wavelength and Z_H [$\text{mm}^6 \cdot \text{m}^{-3}$] is the radar equivalent reflectivity factor (sometimes expressed in logarithmic power (dBZ) and often simply referred to as reflectivity). The parameter K_a is the ash complex dielectric factor of ash particles defined as

$$|K_a|^2 = \left| \frac{\varepsilon_{ra} - 1}{\varepsilon_{ra} + 2} \right|^2 = \left| \frac{(\varepsilon'_{ra} - j\varepsilon''_{ra}) - 1}{(\varepsilon'_{ra} - j\varepsilon''_{ra}) + 2} \right|^2 \quad (11)$$

where ε'_{ra} and ε''_{ra} are the real and the imaginary part of the ash relative dielectric constant ε_{ra} . Adams *et al.* [36] estimated the dielectric constant for several ash samples demonstrating that, from S- to K-band, ε'_{ras} and ε''_{ras} of solid ash are basically constant. Within this frequency interval the real part ε'_{ras} ranges from 5.5 to 6.5, while the complex part ε''_{ras} ranges from 0.08 to 0.27. Thus, the solid-ash dielectric factor K_{as} of solid ash can range from about 0.37 to 0.41, basically depending on silicate contents (dielectric constant is slightly higher of about 10% to 20% for ash with lower silicate contents). As a consequence, in weather radar applications observations of volcanic solid ash it is safe to assume $|K_{as}|^2 = 0.39 \pm 0.02$, regardless of composition or wavelength [36]. By comparison, the dielectric factor is 0.93 for water and 0.197 for ice so that solid ash particles are 2.4 times less reflective than liquid water particles and 2 times more reflective than ice particles, for an identical particle size distribution, density and wavelength.

We can further refine our dielectric model of dry ash aggregates following the Gunn–Marshall approach based on the Debye's theory [52]. We can assume partially vesicular ash particles as a mixture of solid ash and air. The ratio K_a/ρ_a of the ash mixture may be assumed equal to the sum of the ratios corresponding to solid ash and air weighted by their relative mass. Since $|K_{\text{air}}|^2 \cong 0$, it yields

$$K_a \cong \frac{\rho_a}{\rho_{as}} \left(\frac{m_{as}}{m_a} \right) K_{as} = \rho_a f_m \left(\frac{\varepsilon_{ras} - 1}{\varepsilon_{ras} + 2} \right) \quad (12)$$

where f_m is the mass fraction of solid over vesicular ash and in the last term of (12) the solid-ash density ρ_{as} has been put equal to $1 \text{ g} \cdot \text{cm}^{-3}$. The complex relative dielectric constant ε_{ra} of vesicular ash can be derived from K_a definition giving $\varepsilon_{ra} = (2K_a - 1)/(K_a - 1)$. If $f_m \cong 1$, from (12) it results that the vesicular ash dielectric factor is $|K_a|^2 = 0.39\rho_a^2$. A further model improvement might be to let ρ_a to be inversely dependent on particle diameter (bigger particles are generally less dense), but to our knowledge there are no experimental data to parameterize this dependence. Other mixing formulas, such as that of Maxwell-Garnet (e.g., [41] and [46]) might be used, but this analysis is beyond our scope.

TABLE II
CLASSES OF AVERAGE ASH SIZE AND CONCENTRATION IN TERMS OF AVERAGE MEAN VALUES OF DIAMETER DEVIATION-MEAN PROPORTIONALITY AND RANGE

Mean diameter D_n [mm]	Average Mean Diameter $\langle D_n \rangle$	Proportionality σ_{D_n} and $\langle D_n \rangle$	Diameter D range
Fine Ash	0.01	20%	0.0064-0.064
Coarse Ash	0.1	20%	0.064-0.64
Lapilli	1.0	20%	0.64-6.4
Ash concentration C_a [g m^{-3}]	Average Concentration $\langle C_a \rangle$	Proportionality σ_{C_a} and $\langle C_a \rangle$	Concentration C_a range
Light	0.1	50%	0.01-0.5
Moderate	1.0	50%	0.5-2.0
Intense	5.0	50%	2.0-8.0

If the ash medium exhibits path attenuation at the chosen wavelength, then specific attenuation or extinction k_H [m^{-1}] can be evaluated from [41], [42]

$$k_H = \int_{D_1}^{D_2} \sigma_{eH}(D) N_a(D) dD \quad (13)$$

where $\sigma_{eH} = \sigma_{sH} + \sigma_{aH}$ [m^2] is the extinction cross section, given by the sum of scattering and absorption cross sections, respectively, at horizontal polarization. Radar observables can be related to volcanic ash parameters by assuming a backscattering and absorption model for the particle ensemble. Analytical relations valid under the Rayleigh assumption of spherical particles much smaller than the radar wavelength may be adequate for ash clouds under some conditions, as we will prove in the next section. Under Rayleigh's approximation, it holds [40], [41]

$$\begin{cases} \sigma_{bH}(D) = \frac{\pi^5 |K_a|^2}{\lambda^4} D^6 \\ \sigma_{eH}(D) = \sigma_{sH}(D) + \sigma_{aH}(D) \\ \quad = \frac{2\pi^5}{3\lambda^4} |K_a|^2 D^6 + \frac{\pi^2}{\lambda} \text{Im}[K_a] D^3. \end{cases} \quad (14)$$

Using (14) and (5), then (10) and (13) become

$$\begin{cases} Z_H = \int_{D_1}^{D_2} D^6 N_a(D) dD = m_6 \\ k_H = \frac{2\pi^5}{3\lambda^4} |K|^2 m_6 + \frac{\pi^2}{\lambda} \text{Im}[K] m_3. \end{cases} \quad (15)$$

The Rayleigh reflectivity factor Z_H is proportional to the sixth power of the particle diameter and, consequently, the larger particles influence the reflectivity factor much more than smaller particles of equal abundance.

From (15) and (7), it is straightforward to derive within each radar range bin an analytical relationship between the radar Rayleigh reflectivity factor Z_H and spherical-ash physical parameters such its concentration C_a

$$Z_H = \left(\frac{6}{\pi \rho_a} \frac{m_6}{m_3} \right) C_a \cong 50.13 \frac{D_n^3}{\rho_a} C_a \quad (16)$$

where the last term is valid only for a SG-PSD with $\mu = 1$, i.e., using (9). Equation (16) tells us that, for a given spherical ash density and concentration, Z_H tends to be stratified with respect to the mean diameter D_n . For a given C_a and D_n , Z_H increases as ρ_a decreases due to the increase of the log-intercept N_n of $N_a(D)$ from (3)—if C_a is constant, decreasing ρ_a means to increase the particle volume from (4). Previous equation may represent a physical relation to convert radar reflectivity into ash parameters if D_n and ρ_a are known.

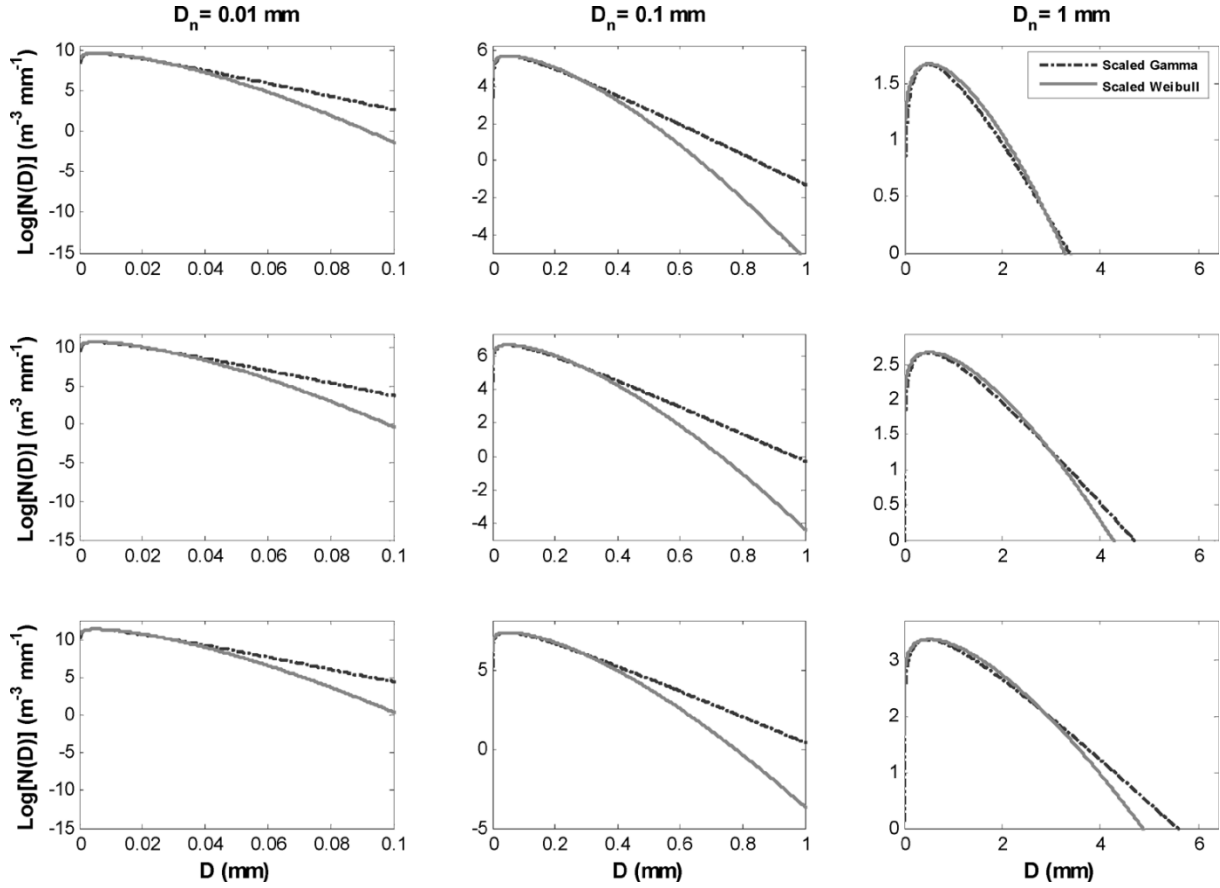


Fig. 3. Average PSD for the nine ash classes, divided into fine ash (left column), coarse ash (middle column), and lapilli (right column) and light (top row), moderate (middle row) and intense (bottom row) ash concentrations, as function of ash diameter for the scaled-Weibull PSD with $\gamma = -0.5$ (continuous line) and for the scaled-Gamma with $\mu = 1$ (dashed line), assuming $\rho_a = 1 \text{ g} \cdot \text{cm}^{-3}$ average values of D_n and C_a are reported in Table II for each class.

IV. NUMERICAL SIMULATIONS OF VOLCANIC ASH RADAR REFLECTIVITY

The knowledge of ash PSD as in (2), together with ash density, composition and shape, allows the numerical simulation of radar reflectivity and extinction using (10) and (13). In order to analyze the sensitivity of radar response to ash parameterization, it is convenient to consider different ash diameter classes and concentration regimes. From Section II and the Appendix, we may note that the driving parameters of an ash PSD have been reduced to D_n , C_a , and μ . Indeed, μ (related to ν for SW-PSD) has been found to be pretty constant depending on the predominant eruption mechanism (i.e., magmatic or hydrovolcanic fragmentation) [32]. In order to generate physically oriented ash classes, we can basically play on D_n and C_a variability. From available literature and ash measurements (see also Section II), we have defined three classes for average ash diameters (fine, coarse, and lapilli) and three classes for average ash concentration regimes (light, moderate, and intense), as in Table II. The average value of ash size in terms of ϕ units for each class can be easily derived from (1) for fine, coarse, and lapilli size classes and are equal to 9.97, 6.64, and 0.00, respectively.

As an example of PSD behavior, Fig. 3 shows, in a logarithm plane, the average PSDs for the nine ash classes, defined in Table II, as function of ash diameter for the scaled-Gamma PSD with $\mu = 1$ and the scaled-Weibull PSD with $\gamma = -0.5$. As expected from (2) and the Appendix, the modal value of each PSD is related to increasing values of D_n . For larger diameters,

TABLE III
RAYLEIGH CONDITIONS IN TERMS OF MAXIMUM AVERAGE ASH DIAMETERS FOR MICROWAVE RADAR OBSERVATIONS OF ASH CLOUDS

Band	Frequency range (GHz)	Wavelength range (cm)	Rayleigh maximum diameter (mm)
L	1- 2	30.0 - 15.0	19.49 - 9.75
S	2 - 4	15.0 - 7.50	9.75 - 4.87
C	4 - 8	7.50 - 3.75	3.57 - 2.44
X	8 - 12	3.75 - 2.50	2.44 - 1.62
Ku	12 - 18	2.50 - 1.67	1.62 - 1.08
K	18- 27	1.67 - 1.11	1.08 - 0.72
Ka	27 - 40	1.11 - 0.75	0.72 - 0.49
V	40 - 75	0.75 - 0.40	0.49 - 0.26
W	75 - 110	0.40 - 0.27	0.26 - 0.18

the value of N_a for SW-PSD tends to be lower than SG-PSD for all ash classes, while for smaller diameters it happens the opposite. Even though not shown in Fig. 3, it is worth noting that the μ parameter modifies both PSD shapes: given C_a and D_n , as μ increases the number of both larger and smaller ash particles decreases with a corresponding increase of medium-size particles. This behavior is much more pronounced for SG-PSD than for SW-PSD. From (15), this difference between the PSDs will reflect in radar backscattering and absorption features. In our simple scheme each microphysically oriented ash class can represent an ensemble of various conditions having in common the average values of both D_n and C_a . The latter parameters may be randomized in order to perform a sensitivity study of radar response to ash clouds. Within each ash class it has been

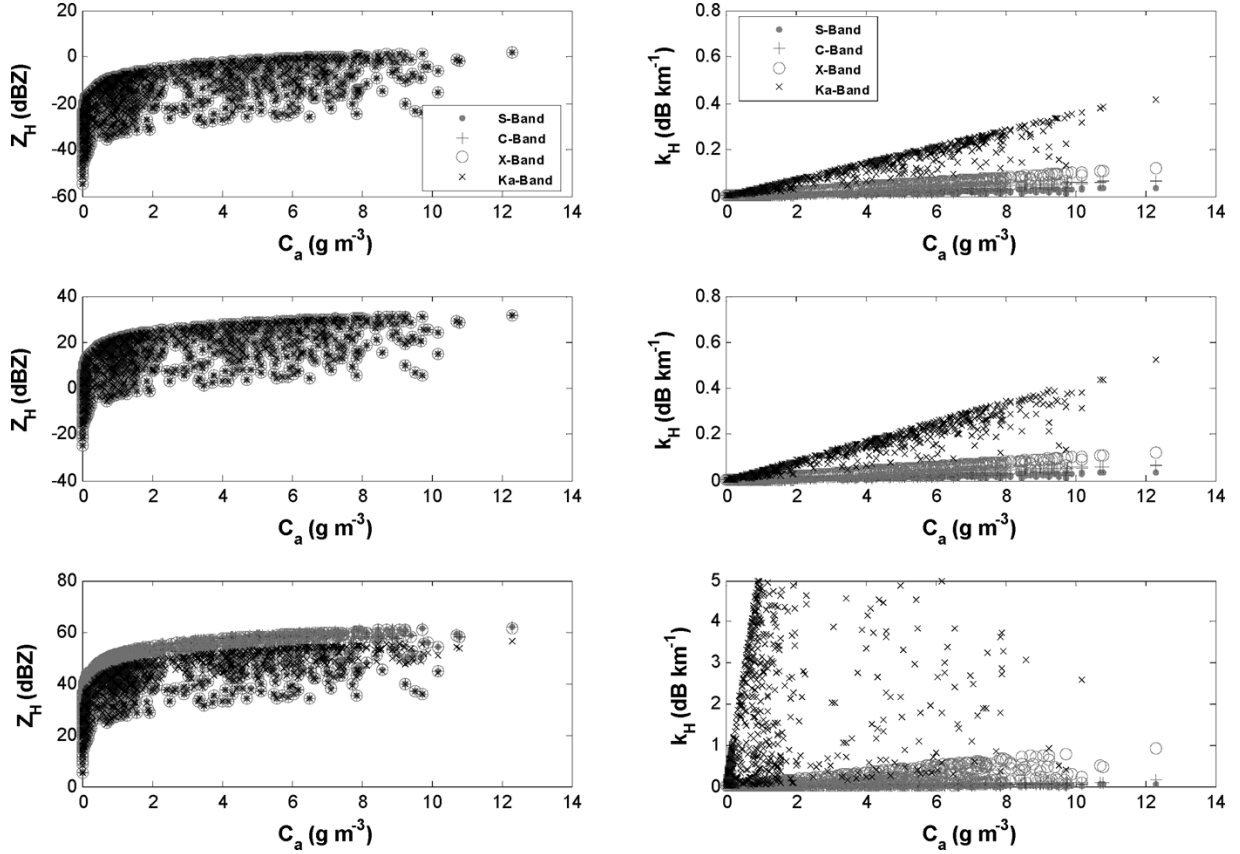


Fig. 4. Scatterplot of simulated horizontally polarized reflectivity factor Z_H (left column) and specific attenuation k_H (right column) versus ash concentration C_a at S-, C-, X-, and Ka-band for the classes of fine ash (top row), coarse ash (middle row), and lapilli (bottom row), defined in Table II, using a scaled-Weibull PSD with $\gamma = -0.5$. Results are obtained assuming $\rho_a = 1 \text{ g} \cdot \text{cm}^{-3}$.

assumed a Gaussian random distribution both for the mean diameter D_n with an average value $\langle D_n \rangle$ and a standard deviation $\sigma_{D_n} = 0.2\langle D_n \rangle$ and for concentration C_a with a mean value $\langle C_a \rangle$ and a standard deviation $\sigma_{C_a} = 0.5\langle C_a \rangle$. The choice of a Gaussian distribution, instead of a uniform one, is mainly related to the aim to categorize ash classes in nine basic classes. As a matter of fact, if we connect this imposed random variability with the average PSDs of Fig. 3, we can realize how the proposed nine ash classes can cover a wide range of ash regimes and be suitable for a sensitivity analysis study.

A. Sensitivity Analysis of Microwave Radar Reflectivity

In Section II we have shown how ground-based weather radar observations at S- and C-band can be used for volcanic ash detection. Other microwave bands may be also used to retrieve ash mass such as X- and Ka-band. A basic question arises whether a Rayleigh model, summarized in (16), may be adopted for ash retrieval at all microwave bands. When this is not true anymore, Mie scattering effects should be taken into account. A quite general criterion to test Rayleigh scattering hypothesis is given by the following threshold formula [46]:

$$D \leq 0.5 \frac{\lambda}{|n_a| \pi} \quad (17)$$

where D is the single particle diameter and n_a the ash index of refraction. Assuming from Section III $|n_a| = 2.45$, Table III shows the values of the upper limit of (17) for a large range of microwave frequencies from L- to W-band. If we compare

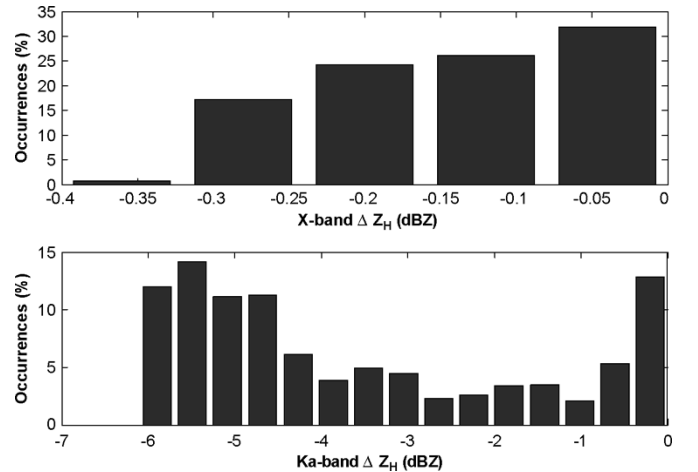


Fig. 5. Histograms of the difference ΔZ_H between Z_H computed using the particle ensemble scattering model and Rayleigh scattering approximation, assuming a scaled-Weibull PSD with $\gamma = -0.5$ for all the nine ash classes, defined in Table II. Plots refer to X-band (top panel) and to Ka-band (bottom panel) with $\rho_a = 1 \text{ g} \cdot \text{cm}^{-3}$. Note that at S- and C-band ΔZ_H is always less than 0.1 dBZ.

Table III with the average mean diameters $\langle D_n \rangle$ of fine ash, coarse ash, and lapilli, given in Table III, we realize that at S-band Rayleigh scattering condition is always well satisfied, at C-band lapilli observations may be affected by Mie effects, while at X-band Rayleigh condition is only valid for fine and coarse ash. Above X-band, Mie effects become no more negligible even for coarse ash. Indeed, two-way path attenuation

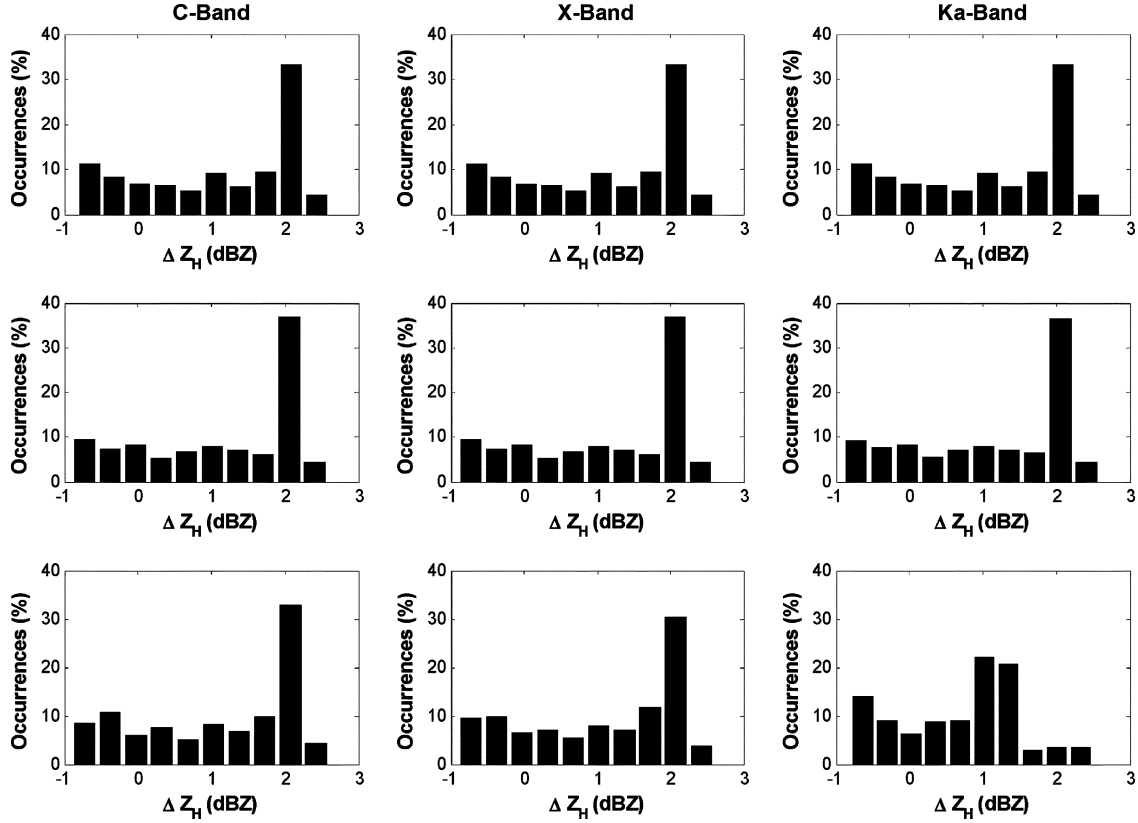


Fig. 6. Histograms of the difference ΔZ_H between Z_H computed from scaled-Gamma PSD with $\mu = 1$ and from scaled-Weibull PSD with $\gamma = -0.5$ for the fine (top-row panels), coarse ash (medium-row panels), and lapilli ash (bottom-row panels), defined in Table II. Plots refer to C-band (left column), X-band (central column), and Ka-band (right column), assuming $\rho_a = 1 \text{ g} \cdot \text{cm}^{-3}$.

has to be also considered at millimeter frequencies as a further impairment which needs to be corrected for before processing reflectivity measurements.

In order to compare in a more detailed way the scattering regimes of the various frequency bands, we have employed a numerical simulator environment called particle ensemble scattering simulator (PESS) [32], [48]. The latter is based on the Mie theory for spherical particle extinction method to compute the complex amplitude scattering matrix \mathbf{S} , which linearly transforms the electric field components of the incident wave into those of the scattered wave [46]–[48]. This simulator can be applied for all scattering regimes evaluating both the reflectivity and specific attenuation in a linearly polarized basis as in (15). Consistently with what already described in Section II, a relative dielectric constant of solid ash equal to $\varepsilon_{ras} = 6 - j0.15$ has been assumed in (12) for all frequency bands—even though experimentally tested up to K-band. The ash density ρ_a has been assumed constant and equal to $1 \text{ g} \cdot \text{cm}^{-3}$ [20]. Incomplete moments m_n in (5) have been computed with D_1 and D_2 given in Table II, even though, when using the complete moments, the discrepancy for Z_H is less than 0.1 dB.

Fig. 4 shows the horizontally polarized reflectivity factor Z_H [in logarithmic power (dBZ)] and specific attenuation k_H at S-, C-, X-, and Ka-band for fine ash, coarse ash, and lapilli as a function of ash concentration, by merging light, moderate, and intense concentration regimes and assuming a scaled-Weibull PSD with $\gamma = -0.5$ and $\rho_a = 1 \text{ g} \cdot \text{cm}^{-3}$. It is worth recalling that, from (15), Rayleigh reflectivity is independent of frequency, while in the Mie region resonance effects give rise to a complicate frequency behavior weighted by PSD (e.g., [40]

and [41]). Note that the nonlinearity between Z_H and C_a is due to the log-scale used for Z_H (see Fig. 8 for comparison).

Note that S-band points are almost covered by C- and X-band ones for all classes. In order to quantify these differences, Fig. 5 shows the difference ΔZ_H between Z_H computed using the PESS scattering model and Rayleigh scattering approximation, assuming a scaled-Weibull PSD with $\gamma = -0.5$ for all the nine ash classes, defined in Table II. Results are only plotted for X- and Ka-band, assuming $\rho_a = 1 \text{ g} \cdot \text{cm}^{-3}$, ΔZ_H at S- and C-band being always less than 0.1 dBZ. From Figs. 5 and 6 we can deduce that the qualitative results derived from Table III are confirmed with a strong difference of radar reflectivity responses only for lapilli observations. For ash concentration of lapilli larger than $5 \text{ g} \cdot \text{m}^{-3}$, differences up to 6 dBZ appear between C- and Ka-band, Ka values being smaller than C-band ones [see (10) and (15)].

For range-resolving instruments such as pulsed radars, path attenuation can be a critical impairment when inverting the reflectivity measurements into geophysical parameters. From Fig. 4, it is demonstrated that for fine and coarse ash k_H is always less than 0.5 dB/km at all bands, being three times higher at Ka-band than at X-band. At S- and C-bands, as expected, path attenuation is always negligible even for intense concentration of lapilli where maximum values are of the order of 0.15 dB/km. At X-band, k_H is less than 0.12 dB/km for coarse ash, but it can be as high as 1 dB/km for intense concentration of lapilli. At Ka-band, path attenuation for lapilli may reach values of several decibels per kilometer.

The impact of modeling ash PSD through the scaled-Gamma PSD with $\mu = 1$ and the scaled-Weibull PSD with $\gamma = -0.5$ is

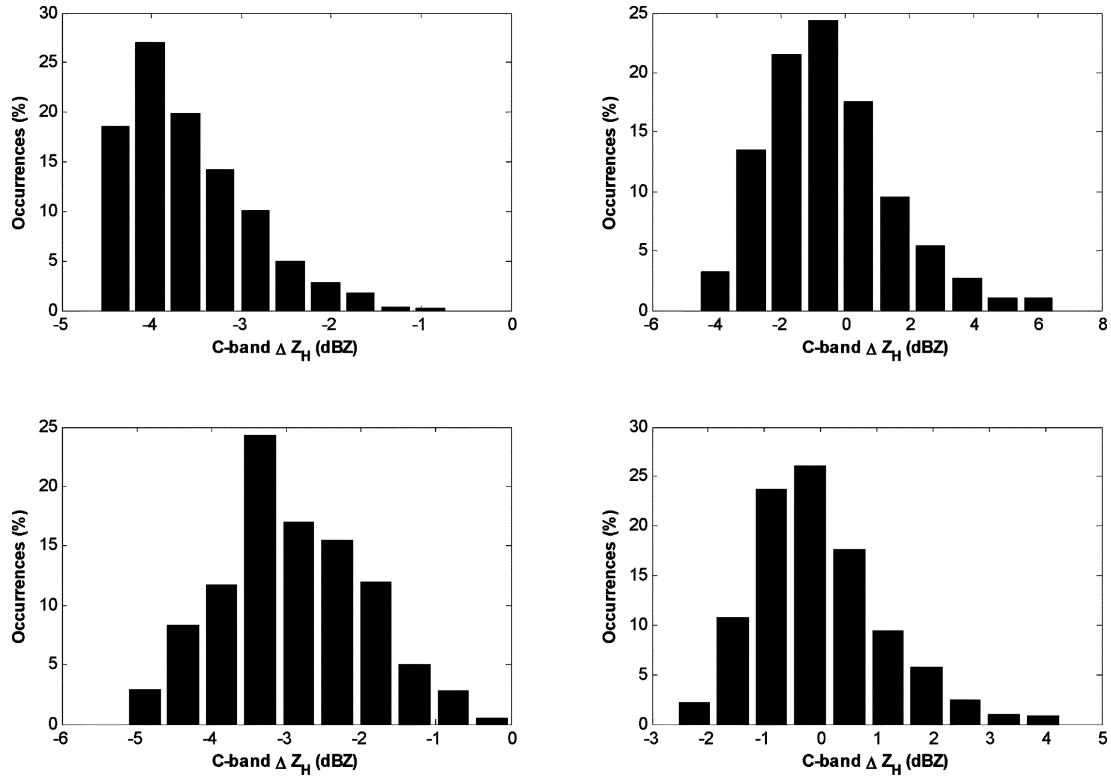


Fig. 7. Histograms of the difference ΔZ_H between Z_H computed from scaled-Weibull PSD with $\gamma = -0.3$ (top left) and with $\gamma = -0.7$ (top right) with respect to the best-fitting case of $\gamma = -0.5$ (see the Appendix) and from scaled-Gamma PSD with $\mu = 3$ (bottom left) and with $\mu = 0$ (bottom right) with respect to the best fitting case of $\mu = 1$ (see the Appendix). These results are for all the nine ash classes, defined Table II and refer to C-band with $\rho_a = 1 \text{ g} \cdot \text{cm}^{-3}$.

shown in Fig. 6. The latter shows the difference ΔZ_H between Z_H computed from scaled-Weibull PSD with $\gamma = -0.5$ and from scaled-Gamma PSD with $\mu = 1$ for all the nine ash classes, defined in Table II. Results refer to C-, X-, and Ka-band, again assuming $\rho_a = 1 \text{ g} \cdot \text{cm}^{-3}$. Values of this difference ΔZ_H are predominantly positive and up to 2.5 dB, meaning that Z_H from scaled-Gamma PSD is larger than that from scaled-Weibull PSD. This behavior may be explained by looking at Fig. 3 where it emerges that SG-PSD tends, for a given C_a and D_n , to attribute particles of larger sizes than those corresponding to SW-PSD. From (15), the importance of larger particles is due to the fact that in a Rayleigh regime PSD contribution to total observed reflectivity is weighted by D^6 , a curve which acts as diameter high-pass filter. Negative values of ΔZ_H are related to low ash concentration of fine ash where the behavior of PSDs is opposite (see Fig. 3). At C-band ΔZ_H histogram is substantially the same for ash size classes, while at Ka-band and for lapilli Mie effects start to be not negligible.

The impact of the PSD shape on radar response is illustrated by Fig. 7. The latter shows the difference ΔZ_H between Z_H computed from scaled-Weibull PSD with $\gamma = -0.3$ and with $\gamma = -0.7$ with respect to the reference case of SW-PSD with $\gamma = -0.5$ and from scaled-Gamma PSD with $\mu = 3$ and with $\mu = 0$ with respect to the reference case of SG-PSD with $\mu = 1$. These results are for all the nine ash classes, defined in Table II and refer to C-band with $\rho_a = 1 \text{ g} \cdot \text{cm}^{-3}$. Histograms of Fig. 8 indicate that as γ increases for SW-PSD, then Z_H tends to decrease—an increase of 40% in γ produces a decrease of about 4 dBZ in Z_H . A decrease of γ gives rise to an average decrease of Z_H of about -0.5 dBZ. This behavior is confirmed for scaled-Gamma PSD so that, for the same value of the other

parameters, the increase of μ tends to give rise to a decrease of average Z_H . These effects are highly nonlinear and not symmetric with respect to the variation of μ in (2) and can be explained keeping in mind the comments, related to Fig. 4, about μ effects on PSD (larger particles increase as μ or γ decreases). The results of Fig. 8 at C-band are basically confirmed when analyzing the other frequency bands.

A further sensitivity analysis has been carried to evaluate the dependence of radar reflectivity on ash density. Values of ρ_a between 0.5 and $2.5 \text{ g} \cdot \text{cm}^{-3}$ were chosen within each ash class for a given C_a and D_n . Results have shown that radar reflectivity up to X-band is sensitive to ρ_a assumptions with a decrease of Z_H of about 3 dBZ for $\rho_a = 2.0 \text{ g} \cdot \text{cm}^{-3}$ with respect to the case of $\rho_a = 1.0 \text{ g} \cdot \text{cm}^{-3}$. At Rayleigh regimes, this can be explained by looking at (16), while for Mie scattering this sensitivity is reduced due to increase of $|K_a|^2$ with the square of ρ_a as deduced from (12).

B. Comparison With Average C-Band Radar Measurements

Microwave radar data of volcanic eruptions are not easy to obtain, the latter being rare events in some specific geographical areas, not always covered by a scanning weather radar. Some of the best reported events are those of March 19, 1982 and Mount Saint Helens eruptions of May 18, 1980 [20].

The eruption of March 19, 1982 started at 19:28 UTC with a small Plinian column associated to a high-amplitude tremor. The major ash eruption was probably produced in a short interval of about 40–50 s. The ash cloud was detected and tracked by the National Weather Service C-band radar, located in Portland, OR. The maximum height of the ash column was

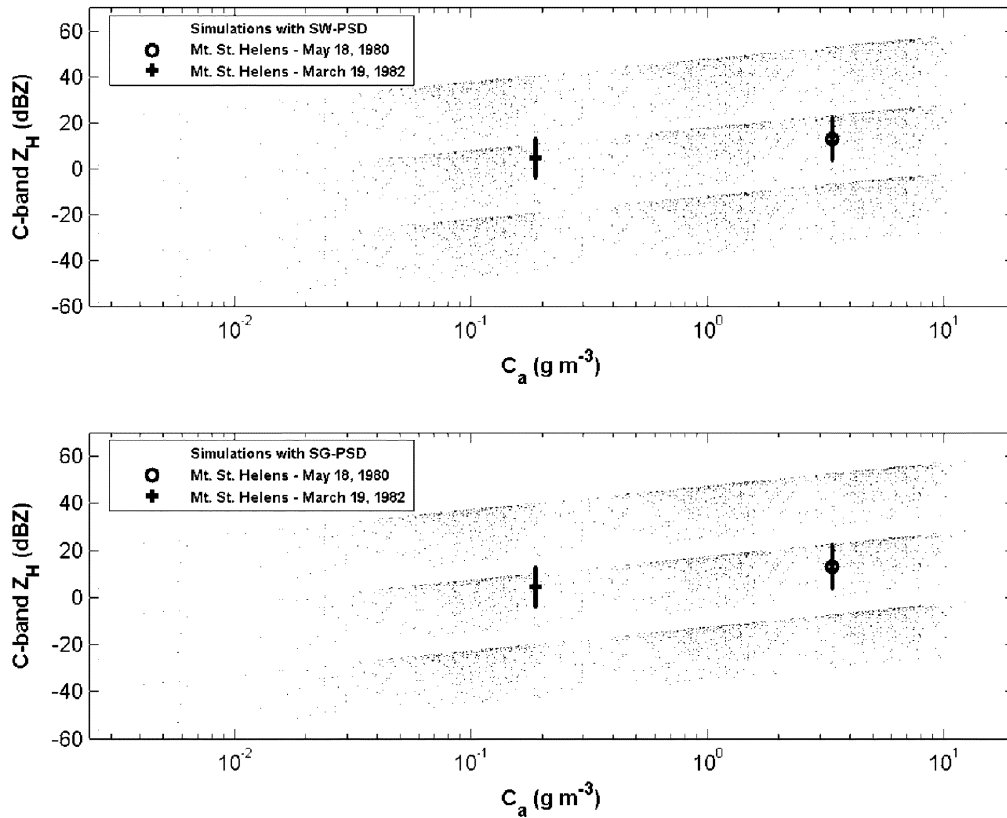


Fig. 8. Scatterplot of simulated C-band reflectivity factor Z_H and ash concentration C_a for the size classes of fine ash, coarse ash, and lapilli, defined in Table II, using a scaled-Weibull (top panel) with $\gamma = -0.5$ and scaled-Gamma with $\mu = 1$ (bottom panel) with $\rho_a = 1 \text{ g} \cdot \text{cm}^{-3}$. “Plus” and “cross” marks show the measured Z_H and C_a derived from Mount Saint Helens eruptions of May 18, 1980 and March 19, 1982, respectively, with an observed variability denoted by the error bars (see text for further details). Both measured and simulated reflectivity data are calibrated with water dielectric factor (i.e., $|K|^2 = 0.93$ in (10); see text for details).

measured at 13.7 km above sea level around 19:38 UTC. This height decreased with time owing to gravitational settling of ash particles, while the root mean square size of the ash cloud was about 15 km. Radar reflectivity factors, inferred from estimated ash PSD, may have been as high as 24.7 dBZ, but would have decreased within 10–20 min to less than 1 dBZ owing to the fallout of particles larger than 1 mm. Between 20:00 and 20:30 UTC measured reflectivity factors were between 0.3 and 8.6 dBZ with an average value of 4.5 dBZ. These Z_H values correspond to an average ash mass concentration of about $0.19 \text{ g} \cdot \text{m}^{-3}$, as derived from deposited ashfall data.

The case study of the eruption on May 18, 1980 was significantly different from that on March 19, 1982. The duration of the Plinian phase was about 9 h. The ash volume of May 18 eruption is a factor 10^3 larger than the one of March 19 and was observed not only from Portland radar, but also from two other aviation radars at 0.7 GHz in Seattle and Spokane (WA). Although the eruption was long lasting, the magma eruption rate was strongly varying with time. The 6-h mean ash concentrations decreased from about $3.7 \text{ g} \cdot \text{m}^{-3}$ at 57 km from the volcano, to lower values at greater distances as the sizes of the largest ash particles decreased due to fallout. Corresponding average reflectivity factors, measured within the same interval of 6 h, were of the order of 13 dBZ with a variability between 8.4 and 17.6 dBZ due probably to ash clusters within the range of 0.2–0.5 mm. Aggregation of fine ash might have caused an enhancement of observed radar reflectivities.

Similarly to Fig. 4, Fig. 8 shows the $Z_H - C_a$ relationship in a logarithmic plane utilizing the scaled-Weibull PSD with

$\gamma = -0.5$ and, for comparison, the scaled-Gamma PSD with $\mu = 1$. Simulated results for the three size classes, defined in Table II (fine ash, coarse ash, and lapilli) are plotted. The labeled marks show average measured reflectivity factor Z_{Hm} and C_a estimated for Mount Saint Helens eruptions of May 18, 1980 (characterized by mean $\langle Z_{Hm} \rangle = 13.0 \text{ dBZ}$ and $\langle C_a \rangle = 3.4 \text{ g} \cdot \text{m}^{-3}$) and March 19, 1982 (characterized by mean $\langle Z_{Hm} \rangle = 4.5 \text{ dBZ}$ and $\langle C_a \rangle = 0.2 \text{ g} \cdot \text{m}^{-3}$). The bars around $\langle Z_{Hm} \rangle$ indicate the observed variability of reflectivity measurements. It is worth mentioning that all meteorological radar are calibrated with the dielectric factor of water, i.e., $|K_w|^2 = 0.93$ in $Z_{Hm} = (P_r r^2)/(C|K_w|^2)$ where P_r is the received power, r the range, and C the radar instrumental constant [40]. From (10), we know that the equivalent reflectivity factor of ash particles is given by $Z_{Ha} = \eta_H(\lambda^4/|K_a|^2\pi^5)$. This means that we need to rescale our Mie scattering simulations of Z_{Ha} into water-equivalent reflectivity factor Z_{Hw} through $Z_{Hw} = Z_{Ha} - 3.77$ in logarithmic power (dBZ) since $|K_a|^2/|K_w|^2 = 0.42$.

The radar measured data refer to places relatively far from the volcano vent and later in time with respect the eruption paroxysm. The Mount Saint Helen measurements seem to be well explained by Rayleigh $Z_H - C_a$ simulations of coarse ash class (with $\langle D_n \rangle = 0.1 \text{ mm}$) both for the May 18, 1980 and for the March 19, 1982 case studies, consistently with ground observations. The ash regimes are, however, quite different, the eruption of 1980 being much more intense than that of 1982 with an average concentration of two orders of magnitude larger. The choice of a particular PSD does not substantially affect this in-

terpretation of the measured results, their differences being well within the ash class variability.

V. CONCLUSION

The potential of using ground-based weather radar systems for volcanic ash cloud detection and quantitative retrieval has been evaluated. In order to do this, a radar response model has been examined taking into account various operating frequencies such as S-, C-, X-, and Ka-bands. After a summary on evidences of weather radar sensitivity to ash clouds, a microphysical characterization of volcanic ash has been carried out.

Particle size-distribution functions have been derived both from sequential fragmentation-transport theory of pyroclastic deposits, leading to a scaled-Weibull PSD, and from more conventional scaled-Gamma PSD functions. Best fitting to PSD available measured data at ground have been shown. The radar backscattering from sphere-equivalent ash particles has been simulated under Rayleigh approximation up to Ka-band, and its accuracy has been assessed by using a T-matrix code. The relationship between radar reflectivity factor, ash concentration, and fall rate has been statistically derived for various eruption regimes and ash median sizes by randomizing key microphysical parameters.

The choice of the optimal radar frequency band might benefit from the results obtained in this work. Basically, C-band may offer some advantages with respect to other bands in terms of radar reflectivity response and negligibility of path attenuation. The latter is tolerable at X-band, but cannot be handled at Ka-band. Indeed, the advantage of higher frequencies, such as X- and Ka band, is the potential reduction of the overall size of the radioelectronic apparatus.

A natural consequence of the results of this work is the development of a prototype algorithm for volcanic ash radar retrieval. For example, adopting approaches developed for spaceborne rain radars [53], from measured single-polarization reflectivity a retrieval of C_a and R_a may be based on two steps: 1) a classification of eruption regime and volcanic ash category; 2) estimation of ash concentration and fall rate. A further model investigation might be oriented to analyze the polarimetric radar response of ash clouds in order to better exploit dual-polarization Doppler radars which are becoming part of the operational network nowadays [54]. Polarimetric radars may offer the advantage to better discriminate the impact of cloud ice and liquid water on ash aggregates. Ash generally nucleates ice early in ash cloud development after emplacement in the high troposphere because magmatic water plus entrained lower tropospheric water is carried upward so that it condenses and freezes. In some ash clouds, this ice rapidly sublimates and disappears in a few hours. But in the early stages of ash cloud formation when coarse ash is present, there is likely to be a lot of ice. Lacasse *et al.* [31] discussed the Hekla eruption case where there was a predominance of ice and where the growth of ice was occurring within the cloud so that the loss of radar signal was probably offset by ice growth.

Future work will be also devoted to the gathering of extensive ash datasets relative to various volcano eruptions in order to better tune the PSD parameters of both scaled-Gamma and scaled-Weibull models. Indeed, ash deposits are an indirect characterization of ash clouds, and in this respect *in situ* ash

measurements should represent the proper validation even though difficult to get. Any ash cloud retrieval algorithm should be then tested against weather radar measurements in a quantitative framework. Recent experimental campaigns and C-band radar measurements in Iceland [31] might represent a unique opportunity in this perspective.

APPENDIX

SIZE DISTRIBUTIONS OF VOLCANIC ASH

The particle size distribution is essential for the evaluation of the backscattering and absorption properties of a particle ensemble. Two basic PSDs have been considered in this work: 1) the Gamma size distribution, mainly as a well-known reference and 2) the Weibull size distribution. These two PSDs are quite general and can describe a wide set of microphysical ash conditions [49]. Note that the log-normal PSD is well represented by a Weibull PSD [44], whereas the inverse exponential PSD is a particular case of Gamma PSD [42].

A. Scaled-Gamma Particle Ash Distribution

The Gamma PSD, conventionally measured in radar meteorology in per millimeter per cubic meter ($\text{mm}^{-1} \cdot \text{m}^{-3}$), assumes the following form [42]:

$$N_G(D) = N_{0G} D^\mu e^{-\Lambda_G D} \quad (\text{A.1})$$

where D is the particle diameter (or equivalent diameter), while N_{0G} , μ , and Λ_G are the so-called intercept, shape, and scale PSD parameters, respectively. Note that N_{0G} has a μ -dependent dimension, while μ is adimensional and Λ_G is in $[\text{mm}^{-1}]$. If the PSD is defined in a semi-infinite positive interval of diameters, that is $D_1 = 0$ and $D_2 = \infty$, then some characteristics parameters of PSD can be easily given in a closed form. From (6) and (7), we can express the number-weighted diameter D_n as

$$D_n = \frac{1}{\Lambda_G} \frac{\Gamma(1 + \mu + 1)}{\Gamma(\mu + 1)} = \frac{\mu + 1}{\Lambda_G} \quad (\text{A.2})$$

where Γ is the complete Gamma function (with $\Gamma(n+1) = n!$ if n is an integer) and, assuming equivalent spheres, the intercept parameter as

$$N_{0G} = \frac{6C_a}{\pi\rho_a} \frac{\Lambda_G^{3+\mu+1}}{\Gamma(3+\mu+1)} = C_a \frac{6}{\pi\rho_a(3+\mu)!} \left[\frac{(\mu+1)!}{D_n(\mu!)} \right]^{3+\mu+1} \quad (\text{A.3})$$

where (A.2) has been used in the last member of (A.3). It is convenient to scale the Gamma PSD by choosing

$$\begin{cases} N_{nG} \equiv N_{0G} D_n^\mu = \frac{6C_a D_n^\mu}{\pi\rho_a(3+\mu)!} \left[\frac{(\mu+1)!}{D_n(\mu!)} \right]^{3+\mu+1} \\ \Lambda_{nG} \equiv \Lambda_G D_n = \mu + 1 \end{cases} \quad (\text{A.4})$$

where (A.2) and (A.3) have been inserted in (A.4). Thus, the scaled-Gamma (SG) particle size distribution can be put in the same form of (2) by setting $\nu = 1$

$$N_{SG}(D; \mu, D_n, C_a) = N_{nG} \left(\frac{D}{D_n} \right)^\mu e^{-\Lambda_{nG} \left(\frac{D}{D_n} \right)}. \quad (\text{A.5})$$

It is worth mentioning that N_{SG} has the following properties.

- N_{nG} , with respect to N_{0G} , has a dimension which is μ -independent and given in [$\text{mm}^{-1} \cdot \text{m}^{-3}$].
- Λ_{nG} is adimensional.
- It is completely specified by the three parameters μ , D_n , and C_a by using (A.4) and assuming an ash constant density ρ_a and spherical (or equivalent-spherical) particles.
- If a finite interval of diameters is used, then incomplete Gamma function, as can be used in place of the complete Gamma function, together with the scaling equation in (A.4) without expressing (A.3) in an explicit way.

The implementation of a SG-PSD with $D_1 = 0$ and $D_2 = \infty$ implies the following steps:

- evaluate the ash density ρ_a ;
- assign D_n and C_a and eventually μ ;
- compute Λ_{nG} from (A.4);
- compute N_{nWG} from (A.4).

The extension of previous procedure to the case of incomplete moments is straightforward using the incomplete Gamma function.

B. Scaled-Weibull Particle Ash Distribution

In the past decade a new approach to the formulation of ash PSD has been proposed by Wohletz *et al.* [33], [43], [44]. This newly developed method of particle size distribution analysis is called sequential fragmentation-transport theory (SFT). Unlike previous methods that were empirically managed, based on for example the Rosin–Rammmler and log-normal PSD, SFT methodology is a physical tool and can predict particle mass distributions formed by a sequence of fragmentation (comminution) and transport (size sorting) events acting upon an initial mass (m'_a). The number distribution $N(m_a)$, in units of particles per unit mass of mass between m_a and $m_a + m'_a$, is expressed by an integral formulation of mass conservation [33]

$$N(m_a) = C \int_0^{\infty} N(m'_a) f(m'_a \rightarrow m) dm'_a \quad (\text{A.6})$$

where f is a transfer function which models the fragmentation effects, and C is a constant, $N(m_a)$ is in [kg^{-1}]. Equation (A.6) represents the summing of all contributions to the distribution at the mass m_a from the fragmentation of all particles, having $m'_a > m_a$ and arising from the fragmentation of a single more massive particle of mass m'_a .

It can be shown that the solution to the integral equation (A.6) is given by [33]

$$N(m_a) = \frac{N_P}{m_w} \left(\frac{m_a}{m_w} \right)^{\gamma} e^{-\left(\frac{m_a}{m_w} \right)^{\gamma+1} \frac{1}{\gamma+1}} \quad (\text{A.7})$$

where m_a is, from (4), the mass of an ash spherical (or equivalent-spherical) particle and N_P is the total number of particles given by

$$N_P \equiv \int_0^{\infty} N(m_a) dm_a \quad (\text{A.8})$$

where a semi-infinite positive interval of diameters has been assumed. The parameter m_w is actually an arbitrary value such that $C = (1/m)w$. The parameter γ is a kind of shape PSD feature, defined between -1 and 0 . The value -3γ can also be interpreted as the fractal dimensional of the set of spherical volumes which describe the distribution of fragments resulting from the fractal fragmentation process [33].

From (6) we have

$$\frac{dC_a}{dD} = \frac{\pi}{6} \rho_a D^3 N_W(D) = \frac{dC_a}{dm_a} \frac{dm_a}{dD} \quad (\text{A.9})$$

where N_W is the ash PSD in [$\text{mm}^{-1} \cdot \text{m}^{-3}$] from SFT we are looking for, and from (4)

$$\frac{dm_a}{dD} = \frac{\pi}{2} \rho_a D^2. \quad (\text{A.10})$$

Since for the total mass M_a we can write

$$\frac{dM_a}{dm_a} = m_a N(m_a) \quad (\text{A.11})$$

then, if ΔV_a is the ash volume, we have

$$\frac{dC_a}{dm_a} = \frac{1}{\Delta V_a} \frac{dM_a}{dm_a} = \frac{1}{\Delta V_a} m_a N(m_a). \quad (\text{A.12})$$

Finally, by substituting in (A.9) we get

$$\frac{\pi}{6} \rho_a D^3 N_W(D) = \frac{\pi}{6} \rho_a D^3 \frac{1}{\Delta V_a} N[m_a] \frac{\pi}{2} \rho_a D^2 \quad (\text{A.13})$$

or, by setting $N_t = N_P / \Delta V_a$ and substituting m_a

$$N_W(D) = \left(\frac{\pi}{2} \frac{\rho_a N_t}{m_w} \right) D^2 \left(\frac{\pi}{6} \frac{\rho_a D^3}{m_w} \right)^{\gamma} e^{-\frac{\left(\frac{\pi}{6} \rho_a D^3 \right)^{\gamma+1}}{\gamma+1}}. \quad (\text{A.14})$$

The previous equation can be rewritten in the following compact form:

$$N_W(D) = N_{0W} D^{\mu} e^{-\Lambda_W D^{\mu+1}} \quad (\text{A.15})$$

where

$$\begin{aligned} \mu &= 3\gamma + 2 \\ N_{0W} &= 3 \left(\frac{\pi}{6} \frac{\rho_a}{m_w} \right)^{\gamma+1} N_t \\ \Lambda_W &= \left(\frac{\pi}{6} \frac{\rho_a}{m_w} \right)^{\gamma+1} \frac{1}{\gamma+1}. \end{aligned} \quad (\text{A.16})$$

Equation (A.15) represents a Weibull PSD as the power μ of the second factor D^{μ} is one less than the power of the exponent argument $D^{\mu+1}$.

In order to introduce a physical interpretation of the Weibull PSD, we can compute its complete moment of order n , i.e.,

$$m_n = \frac{N_{0W} \Lambda_W^{\frac{n+\mu+1}{\mu+1}}}{(\mu+1)} \Gamma \left(1 + \frac{n}{\mu+1} \right) \quad (\text{A.17})$$

so that, from (6), the ash concentration C_a is given by

$$C_a = \left(\frac{\pi \rho_a}{6} \right) \frac{N_{0W} \Lambda_W^{\frac{-(\mu+4)}{(\mu+1)}}}{(\mu+1)} \Gamma \left(1 + \frac{3}{\mu+1} \right) \quad (\text{A.18})$$

and number-weighted mean diameter D_n , from (7), is expressed by

$$D_n = \Lambda_W^{-\frac{1}{\mu+1}} \Gamma \left(1 + \frac{1}{\mu+1} \right) \\ = \left(\frac{\pi \rho_a}{6 m_w} \right)^{-\frac{1}{3}} (\gamma+1)^{\frac{1}{3(\gamma+1)}} \Gamma \left(1 + \frac{1}{3(\gamma+1)} \right). \quad (\text{A.19})$$

Note that the average mass $\langle m_a \rangle$ is defined as follows:

$$\langle m_a \rangle = \frac{\int_0^\infty m_a N(m_a) dm_a}{\int_0^\infty N(m_a) dm_a} = m_w (\gamma+1)^{\frac{1}{(\gamma+1)}} \Gamma \left(1 + \frac{1}{\gamma+1} \right) \quad (\text{A.20})$$

which shows the relation between $\langle m_a \rangle$ and m_w . Finally, in a way similar to (A.4), by scaling the PSD parameters as follows:

$$\begin{cases} N_{nW} \equiv N_{0W} D_n^\mu \\ \Lambda_{nW} \equiv \Lambda_W D_n^{\mu+1} = \left(\frac{\pi \rho_a}{6 m_w} \right)^{\gamma+1} \frac{D_n^{\mu+1}}{\gamma+1} \end{cases} \quad (\text{A.21})$$

the scaled-Weibull (SW) particle size distribution can be put in the same form of (2) by setting $\nu = \mu + 1$

$$N_{SW}(D; \mu, D_n, C_a) = N_{nW} \left(\frac{D}{D_n} \right)^\mu e^{-\Lambda_{nW} \left(\frac{D}{D_n} \right)^{\mu+1}}. \quad (\text{A.22})$$

We note that for $\mu = 0$ or $\gamma = -2/3 = -0.66$, the scaled-Weibull PSD reduces to an inverse exponential PSD.

In summary, the implementation of a SW-PSD with $D_1 = 0$ and $D_2 = \infty$ implies the following steps.

- Evaluate the ash density ρ_a .
- Assign D_n and C_a and eventually μ .
- Compute γ from (A.16).
- Compute m_w from (A.19) and Λ_{nW} from (A.21), summarized by the following compact expressions:

$$\Lambda_{nW} = \Lambda_W D_n^{3(\gamma+1)} = \left[\Gamma \left(1 + \frac{1}{3(\gamma+1)} \right) \right]^{3(\gamma+1)}. \quad (\text{A.23})$$

- Compute N_{0W} from (A.18) and then N_{nW} from (A.21) summarized in the following compact expressions:

$$N_{nW} = N_{0W} D_n^\mu \\ = N_{0W} D_n^{3\gamma+2} \\ = \frac{18(\gamma+1) \left[\Gamma \left(1 + \frac{1}{3(\gamma+1)} \right) \right]^{3(\gamma+2)} C_a D_n^{-4}}{\pi \rho_a \Gamma \left(1 + \frac{1}{(\gamma+1)} \right)}. \quad (\text{A.24})$$

C. Parameterization by Experimental Data Best Fitting

The best fit of a measured PSD $N_m(D)$ can be accomplished by choosing either a scaled-Gamma PSD or a scaled-Weibull PSD. By assuming μ as an integer for simplicity, the best fitting procedure to find the optimal value of μ , and then $N_a(D)$ suggests the following steps.

- 1) Estimate the ash concentration C_a from (7)

$$\hat{C}_a \equiv \int_0^\infty m_a(D) N_m(D) dD = \frac{\pi}{6} \rho_a \hat{m}_3. \quad (\text{A.25})$$

- 2) Estimate the number-weighted mean diameter D_n from (8)

$$\hat{D}_n = \frac{\int_0^\infty D N_m(D) dD}{\int_0^\infty N_m(D) dD} = \frac{\hat{m}_1}{\hat{m}_0}. \quad (\text{A.26})$$

- 3) Estimate the intercept N_n and the slope Λ_n of the chosen PSD expressed in (2), as prescribed from (A.4) for SG and (A.23) and (A.24) for SW.
- 4) Minimize, in a likelihood sense, the square difference between the measured $N_m(D)$ and the scaled PSD $N_a(D; \mu)$ in order to find the best μ

$$\hat{\mu} = \text{Min} \left\langle \left[\sum_{i=1}^{N_D} \left(N_a \left(\frac{D_i}{D_n} \right)^\mu e^{-\Lambda_n \left(\frac{D_i}{D_n} \right)^\nu} - N_m(D_i) \right) \right]^2 \right\rangle \quad (\text{A.27})$$

where the ensemble average, indicated by angle brackets, is extended to all $N_m(D)$ available measurements and N_D is the number of diameter bins centered in D_i .

When using a scaled-Gamma PSD model for N_a in (A.27) and letting μ to vary between 0 and 6, the analysis of available measured PSDs from Harris and Rose dataset [20] led to the result that the most probable value of μ is about 1 (with a degree of confidence of about 95%). Indeed, values of μ of about 2 for ash Gamma PSD are also reported in literature (e.g., [29]). The same result of $\mu = 1$ has been derived by analyzing Mount Etna's available ash data [50]. This ash deposit was collected on July 22, 1998 at ground at various distances from the volcano vent, going from Torre del Filosofo site at 1.6 km up to Catania at 27.4 km and Agnone site at 49 km. This eruption of July 1998 belongs to the summit eruption cycle of Mount Etna volcano, initiated after the end of the 1991–1993 eruption and listed among the most complex events in the recent history of Etna. All four summit craters produced spectacular and powerful activity, ranging from mild persistent Strombolian and slow effusive activity over lava fountaining to high-energy explosive episodes and lava overflow from all four summit craters as well as from fissures near the southeastern crater. A period of spectacular eruptive activity in the Voragine location lasted during June–September 1998, culminating in a powerful eruptive episode on July 22, 1998 (and a slightly lesser one on August 6, 1998). The behavior of the collected ash PSD deposit with distance clearly show the sorting mechanism of ash-fall such that large ash particles decrease in volumetric number as the distance increase due to the fallout.

When using a scaled-Weibull PSD within the best fitting procedure of (A.27), the optimal value of γ has been found to be about -0.5 [i.e., $\mu = 0.5$ in (2)] for both available datasets of Mount Saint Helen and Mount Etna with a degree of confidence of about 95%. Interestingly this value is consistent with what found in volcanologic literature and suggested by the segmentation and fragmentation theory [33].

ACKNOWLEDGMENT

The authors are grateful to R. Hannelsen (AMS-Gematronik, Germany) for having provided helpful discussions on radar system requirements. The authors also thank Meteo France and NATO Sigonella base for providing radar imagery. The

intense cooperation of G. Ferrauto and E. Picciotti (CETEMPS, L'Aquila, Italy) throughout this work is also gratefully acknowledged. Useful interactions with J. Taddeucci (INGV, Rome, Italy) have been highly appreciated.

REFERENCES

- [1] L. Wilson, "Explosive volcanic eruptions," *J. Geophys. Res.*, vol. 30, pp. 381–392, 1972.
- [2] L. Wilson, R. S. J. Sparks, T. C. Huang, and N. D. Watkins, "The control of volcanic column height by eruption energetics and dynamics," *J. Geophys. Res.*, vol. 83, pp. 1829–1836, 1978.
- [3] B. Zimanowski, K. Wohletz, P. Dellino, and R. Buttner, "The volcanic ash problem," *J. Volcanol. Geothermal Res.*, vol. 122, pp. 1–5, 2003.
- [4] W. I. Rose, "Interaction of aircraft and explosive eruption clouds: A volcanologist's perspective," *AIAA J.*, vol. 25, pp. 52–58, 1986.
- [5] T. J. Casadevall, "Volcanic ash and aviation safety," *U.S. Geol. Surv. Bull.*, no. 2047, pp. 450–469, 1994.
- [6] J. R. Riehle, W. I. Rose, D. J. Schneider, T. J. Casadevall, and J. S. Langford, "Unmanned aerial sampling of a volcanic ash cloud," *EOS Trans. Amer. Geophys. Union*, vol. 75, no. 12, pp. 137–138, 1994.
- [7] W. I. Rose and D. J. Schneider, "Satellite images offer aircraft protection from volcanic ash clouds," *EOS Trans. Amer. Geophys. Union*, vol. 77, pp. 529–532, 1996.
- [8] T. P. T. P. Miller and T. J. Casadevall, "Volcanic ash hazards to aviation," in *Encyclopaedia of Volcanology*, H. Sigurdsson, Ed. San Diego, CA: Academic, 2000, pp. 915–930.
- [9] W. I. Rose, G. J. S. Bluth, and G. G. J. Ernst, "Integrating retrievals of volcanic cloud characteristics from satellite remote sensors—A summary," *Phil. Trans. R. Soc. A*, vol. 358, no. 1770, pp. 1585–1606, 2000.
- [10] R. E. Holasek and S. Self, "GOES weather satellite observations and measurements of the May 18, 1980 Mount St. Helens eruption," *J. Geophys. Res.*, vol. 100, pp. 8469–8467, 1995.
- [11] D. W. Hillger and J. D. Clark, "Principal component image analysis of MODIS for volcanic ash. Part I: Most important bands and implications for future GOES imagers," *J. Appl. Meteorol.*, vol. 41, pp. 985–1001, 2002.
- [12] T. Yu, W. I. Rose, and A. J. Prata, "Atmospheric correction for satellite-based volcanic ash mapping and retrievals using split-window IR data from GOES and AVHRR," *J. Geophys. Res.*, vol. 107, no. D16, p. 4311, 2002.
- [13] A. J. Prata, "Infrared radiative transfer calculations for volcanic ash clouds," *Geophys. Res. Lett.*, vol. 16, pp. 1293–1296, 1989.
- [14] —, "Observations of volcanic ash clouds in the 10–12 micrometer window using AVHRR/2 data," *Int. J. Remote Sens.*, vol. 10, no. 3 and 4, pp. 751–761, 1989.
- [15] S. Wen and W. I. Rose, "Retrieval of sizes and total masses of particles in volcanic clouds using AVHRR bands 4 and 5," *J. Geophys. Res.*, vol. 99, pp. 5421–5431, 1994.
- [16] N. A. Krotkov, O. Torres, C. Sefor, A. J. Drueger, A. Kostinski, W. I. Rose, G. J. S. Bluth, D. J. Schneider, and S. J. Schaefer, "Comparison of TOMS and AVHRR volcanic ash retrievals from the August 1992 eruption of Mt. Spurr," *Geophys. Res. Lett.*, vol. 26, pp. 455–458, 1999.
- [17] C. J. Sefor, N. C. Hsu, J. R. Herman, P. K. Bhartia, O. Torres, W. I. Rose, D. J. Schneider, and N. Krotkov, "Detection of volcanic ash clouds from Nimbus-7/TOMS," *J. Geophys. Res.*, vol. 102, pp. 16 749–16 760, 1997.
- [18] D. J. Delene, W. I. Rose, and N. C. Grody, "Remote sensing of volcanic clouds using special sensor microwave imager data," *J. Geophys. Res.*, vol. 101, pp. 11 579–11 588, 1996.
- [19] D. M. Harris, W. I. Rose, R. Roe, and M. R. Thompson, "Radar observations of ash eruptions at Mount St. Helens volcano, Washington," *U.S. Geol. Surv. Bull.*, no. 1250, pp. 323–334, 1981.
- [20] D. M. Harris and W. I. Rose, "Estimating particle sizes, concentrations and total mass of ash in volcanic clouds using weather radar," *J. Geophys. Res.*, vol. 88, pp. 10 969–10 983, 1983.
- [21] M. D. Krohn, L. R. Lemon, and J. Perry, "WSR-88D applications to volcanic ash detection," in *Proc. 1st Nat. NEXRAD Users Conf.*, Norman, OK, Oct. 1994.
- [22] W. I. Rose and A. B. Kostinski, "Radar remote sensing of volcanic clouds," in *U.S. Geol. Surv. Bull.: Proc. Int. Symp. Volcanic Ash and Aviation Safety*, vol. 2047, T. Casadevall, Ed., 1994, pp. 391–396.
- [23] W. I. Rose, A. B. Kostinski, and L. Kelley, "Real time C band radar observations of 1992 eruption clouds from Crater Peak/Spurr volcano, Alaska," in *U.S. Geol. Surv. Bull.: Spurr Eruption*, 1995, pp. 19–26.
- [24] B. Stunder and J. Hefftor, "Modeling volcanic ash transport and dispersion," in *U. S. Geol. Surv. Bull.: Proc. Int. Symp. Volcanic Ash and Aviation Safety*, vol. 2047, T. Casadevall, Ed., 1994, pp. 277–282.
- [25] M. Favalli, F. Mazzarini, M. T. Pareschi, and E. Boschi, "Role of local wind circulation in plume monitoring at Mt. Etna volcano (Sicily): Insights from a mesoscale numerical model," *Geophys. Res. Lett.*, vol. 31, 2004. DOI: 10.1029/2003GL019281.
- [26] G. Dubosclard, R. Cordesses, P. Alard, C. Hervier, M. Coltelli, and J. Kornprobst, "First testing of a Volcano Doppler Radar (Voldorad) at Mt. Etna," *J. Geophys. Res.*, vol. 26, pp. 3389–3392, 1999.
- [27] N. Houlié, P. Briole, A. Nercessian, and M. Murakami, "Sounding the plume of the 18 August 2000 eruption of Miyakejima volcano (Japan) using GPS," *Geophys. Res. Lett.*, vol. 32, no. L05302, 2005. DOI:10.1029/2004GL021728.
- [28] G. P. Gobbi, F. Congeduti, and A. Ariani, "Early stratospheric effects of the Pinatubo eruption," *Geophys. Res. Lett.*, vol. 19, pp. 997–1000, 1992.
- [29] M. Maki, K. Iwanami, R. Misumi, R. J. Doviak, T. Wakayama, K. Hata, and S. Watanabe, "Observation of volcanic ashes with a 3-cm polarimetric radar," in *Proc. 30th Radar Meteorological Conf.*, 2001, P5.13.
- [30] M. Maki and R. J. Doviak, "Volcanic ash size distribution determined by weather radar," in *Proc. IGARSS*, Sydney, Australia, Jul. 9–13, 2001, pp. 1810–1811.
- [31] C. Lacasse, S. Karlsdóttir, G. Larsen, H. Soosalu, W. I. Rose, and G. G. J. Ernst, "Weather radar observations of the Hekla 2000 eruption cloud," *Iceland. Bull. Volcanol.*, vol. 66, pp. 457–473, 2004.
- [32] F. S. Marzano, E. Picciotti, G. Ferrauto, G. Vulpiani, and W. I. Rose, "Volcanic ash remote sensing by ground-based microwave weather radar," in *Proc. EGU05 General Assembly*, Apr. 25–29, 2005.
- [33] K. H. Wohletz, M. F. Sheridan, and W. K. Brown, "Particle size distributions and the sequential fragmentation/transport-theory applied to volcanic ash," *Geophys. Res. Lett.*, vol. 16, pp. 15 703–15 721, 1989.
- [34] J. S. J. S. Gilbert and S. J. Lane, "The origin of accretionary lapilli," *Bull. Volcanol.*, vol. 56, pp. 398–411, 1994.
- [35] C. M. Riley, W. I. Rose, and G. J. S. Bluth, "Quantitative shape measurements of distal volcanic ash," *J. Geophys. Res.*, vol. 108, no. B10, pp. 2504–2514, 2003.
- [36] R. Adams, W. F. Perger, W. I. Rose, and A. Kostinski, "Measurements of the complex dielectric constant of volcanic ash from 4 to 19 GHz," *J. Geophys. Res.*, vol. 101, pp. 8175–8185, 1996.
- [37] O. Munoz, H. Volten, J. W. Hovonier, B. Vehelmann, W. J. van der Zande, L. B. F. M. Waters, and W. I. Rose, "Scattering matrices of volcanic ash particles of Mount St. Helens, Redoubt, and Mount Spurr volcanoes," *J. Geophys. Res.*, vol. 109, no. D16201, pp. 1–16, 2004.
- [38] S. Young, R. S. J. Sparks, R. Robertson, L. Lynch, and W. Aspinall, "Eruption of Soufriere Hills volcano in Montserrat continues," *EOS*, vol. 78, pp. 401–409, 1997.
- [39] F. S. Marzano, E. Picciotti, G. Ferrauto, and G. Vulpiani, "Volcanic ash radar retrieval: A numerical study," Univ. L'Aquila, L'Aquila, Italy, CETEMPS Int. Rep. 6/04, Jun. 2004.
- [40] H. Sauvageot, *Radar Meteorology*. Norwell, MA: Artech House, 1992.
- [41] V. N. Bringi and V. Chandrasekar, *Polarimetric Doppler Weather Radar: Principles and Applications*. Cambridge, U.K.: Cambridge Univ. Press, 2001.
- [42] C. W. Ulbrich, "Natural variations in the analytical form of the raindrop size distribution," *J. Clim. Applied Meteorol.*, vol. 22, pp. 1764–1775, 1983.
- [43] W. K. Brown and W. K. Wohletz, "A theory of sequential fragmentation and its astronomical applications," *J. Astrophys. Astron.*, vol. 10, pp. 89–112, 1989.
- [44] —, "Derivation of the Weibull distribution based on physical principles and its connection to the Rosin-Rammler and lognormal distributions," *J. Appl. Phys.*, vol. 78, pp. 2758–2763, 1995.
- [45] L. Wilson, "Explosive volcanic eruptions—II the atmospheric trajectories of pyroclasts," *Geophys. J. R. Astron. Soc.*, vol. 30, pp. 381–192, 1972.
- [46] F. T. Ulaby, R. K. Moore, and A. K. Fung, *Microwave Remote Sensing*. Reading, MA: Addison-Wesley, 1981, vol. 1, Fundamentals and Radiometry.
- [47] M. I. Mishchenko, L. D. Travis, and D. W. Mackowski, "T-matrix computations of light scattering by nonspherical particles: A review," *J. Quant. Spectrosc. Radiat. Transf.*, vol. 55, pp. 535–575, 1996.
- [48] G. Vulpiani, F. S. Marzano, V. Chandrasekar, and R. Uijlenhoet, "Model-based iterative approach to polarimetric radar rainfall estimation in presence of path attenuation," *Adv. Geosci.*, vol. 2, pp. 51–57, 2005.

- [49] F. S. Marzano, G. Ferrauto, G. Vulpiani, and E. Picciotti, "Characterization of ash particle size distribution," Univ. L'Aquila, L'Aquila, Italy, CETEMPS Int. Rep. 1/04, Jan. 2004.
- [50] M. Coltelli and S. Scollo, "Eruptive plumes at Mt Etna," presented at the *2nd Int. Workshop on Remote Sensing of Volcanic Eruption Clouds*, Houghton, MI, Jun. 8–12, 2003.
- [51] Y. Sawada, "Eruption cloud echo measured with C-band weather radar," presented at the *2nd Int. Conf. Volcanic Ash and Aviation Safety*, Alexandria, VA, Jun. 21–24, 2004.
- [52] J. S. Marshall and R. Gunn, "Measurements of snow parameters by radar," *J. Meteorol.*, vol. 9, pp. 322–327, 1952.
- [53] F. S. Marzano, A. Mugnai, G. Panegrossi, N. Pierdicca, E. A. Smith, and J. Turk, "Bayesian estimation of precipitating cloud parameters from combined measurements of spaceborne microwave radiometer and radar," *IEEE Trans. Geosci. Remote Sens.*, vol. 37, no. 1, pp. 596–613, Jan. 1999.
- [54] R. J. Doviak, V. Bringi, A. Ryzhkov, A. Zahrai, and D. Zrnica, "Considerations for polarimetric upgrades to operational WSR-88D radars," *J. Atmos. Oceanic Technol.*, vol. 17, pp. 257–278, 1998.



Frank Silvio Marzano (S'89–M'99–SM'03) received the laurea degree (cum laude) in electrical engineering and the Ph.D. degree in applied electromagnetics, in 1988 and 1993, respectively, both from the University of Rome "La Sapienza," Rome, Italy.

He joined the Department of Electronic Engineering, University of Rome "La Sapienza," in 2005, where he teaches courses on antennas, propagation, and remote sensing. In 1993, he collaborated with the Institute of Atmospheric Physics (CNR), Rome. From 1994 until 1996, he was with the Italian Space

Agency, Rome, as a Post-Doctorate Researcher. After being a Lecturer at the University of Perugia, Perugia, Italy, in 1997, he joined the Department of Electrical Engineering, University of L'Aquila, where he is still coordinating the Satellite and Radar Remote Sensing Laboratory. His current research interests are passive and active remote sensing of the atmosphere from ground-based, airborne, and spaceborne platforms, with a particular focus on precipitation using microwave and infrared data, development of inversion methods, radiative transfer modeling of scattering media, and radar meteorology issues. He is also involved in radiopropagation topics in relation to incoherent wave modeling, scintillation prediction, and rain fading analysis along satellite microwave links. He has published more than 45 papers in refereed international journals and books and more than 170 extended abstract in international and national congress proceedings.

Dr. Marzano received the Young Scientist Award of the XXIV General Assembly of the International Union of Radio Science in 1993. In 1998, he was the recipient of the Alan Berman Publication Award from the Naval Research Laboratory, Washington, DC. Since 2001, he is the Italian National Delegate for the European COST actions number 720 on meteorological remote sensing and number 280 on satellite communications. He is an Associate Editor for IEEE GEOSCIENCE AND REMOTE SENSING LETTERS. In 2004, he was Co-Guest Editor of the special issue on MicroRad04 for IEEE TRANSACTIONS ON GEOSCIENCE AND REMOTE SENSING.



Gianfranco Vulpiani received the laurea and Ph.D. degrees in physics from the University of L'Aquila, L'Aquila, Italy, in 2001 and 2005, respectively.

In 2001, he joined the Department of Physics and the Center of Excellence (CETEMPS), University of L'Aquila as a Research Scientist on ground-based radar meteorology, with a special focus on C-band applications. In 2004, he was a Visiting Student at the Colorado State University (CSU). His current research concerns active remote sensing of the atmosphere from ground-based sensors, with a particular focus on development of polarimetric precipitation retrieval techniques.

Dr. Vulpiani is a reviewer for several international journals in remote sensing topics.

William I. Rose received the Ph.D. degree in geology from Dartmouth College, Hanover, NH, in 1970.

He is currently a Professor of geology at Michigan Technological University, Houghton, where he has worked on volcanic ash research for 34 years. His earliest professional work extended his graduate studies in gas and ash emission studies in Central America, and expanded to Indonesia, Washington, Hawaii, and Antarctica. In the 1980s, he began developing an interest in the potential aircraft hazards from volcanic clouds, years ahead of any serious scientific efforts toward this issue. With more than 150 published papers on volcanic studies, he has investigated multispecies and regional gas measurements of volcanic emissions, ash–aerosol interactions, aircraft hazards, distal ash fallout patterns, quantitative retrievals of ash particles, and detection of ice in volcanic clouds. He developed the first methodology to use infrared satellite data for quantitative retrievals of ash particles, size, and cloud mass: his ground-breaking work, with his graduate student S. Wen, in 1994, formed the basis for current methods of infrared retrieval of ash particles. His latest work is toward merging multisensor retrievals of volcanic clouds, deriving simultaneous data of ash, aerosol, and gas species. He has led efforts to develop new monitoring and analytical tools with a variety of sensors and has published valuable syntheses of remote sensing studies.

Dr. Rose is a member of the International Association of Volcanology and Chemistry of the Earth's Interior and a Fellow of the Geological Society of America and the American Geophysical Union.